73rd International Astronautical Congress (IAC), Paris, France, 18-22 September 2022.

IAC-22-B2.1.4.x72065

Lunar Surface exploration based on LCNS orbiters and Onboard Sensor observables

Giuseppe Tomasicchio[a*], Anna Maria Gargiulo[b], Antonio Genova[b], Maria Marsella[b], Simone Andolfo[b], Edoardo Del Vecchio[b], Flavio Petricca[b], Filippo Rodriguez[a], Carlo Albanese[a]

[a] *Telespazio SpA (giuseppe.tomasicchio@telespazio.com, filippo.rodriguez@telespazio.com carlo.albanese@telespazio.com)*
[b] *Sapienza University of Rome, Italy (annamaria.gargiulo@uniroma1.it, antonio.genova@uniroma1.it, maria.marsella@uniroma1.it, simone.andolfo@uniroma1.it, edoardo.delvecchio@uniroma1.it, flavio.petricca@uniroma1.it)*
* Corresponding Author

Abstract

Lunar exploration is a strategic priority to develop and experiment technologies that will pave the way for the future missions to Mars and to other celestial bodies of the Solar System. Robots are expected to prepare the return of humans to the Moon by surveying landing sites, demonstrating *in situ* resource utilization (ISRU), and expanding our access capabilities to difficult areas, *i.e.*, craters and caves. Succeeding in these challenging tasks requires reliable and efficient navigation and communication capabilities. Therefore, space agencies are encouraging the development of a Lunar Communication and Navigation Service (LCNS) to efficiently support lunar assets. A dedicated LCNS infrastructure would lead to unprecedent advantages in future missions by enabling a constant contact with Earth, even in case of Direct To Earth (DTE) link unavailability, *e.g.*, on the far side of the Moon.

To fulfil critical tasks, such as obstacle avoidance, instrument manoeuvring and reaching a precise location on the map, rover near real time positioning is a key requirement. Thus, in our work we investigate a method based on the Extended Kalman Filter (EKF) that implements a multi modal sensor fusion approach to estimate the rover's position and velocity by using observables collected by onboard sensors or provided by a LCNS constellation. We focus on a realistic mission scenario in the Moon's south polar region that includes a robotic vehicle hosting onboard sensors to estimate the travelled distances (Wheel Odometry, WO) and the heading variation (Inertial Measurement Unit, IMU). Furthermore, the LCNS orbiters are supposed to broadcast one-way radio signals that the rover user terminal can detect and exploit, providing GNSS-like functionalities. The rover's localization is accomplished through dead-reckoning during LCNS visibility gaps, by using IMU and WO data and accurate Digital Elevation Models (DEMs) of the lunar surface. Whenever pseudorange and pseudorange rate data are acquired by the rover LCNS terminal, these measurements are processed by the navigation filter in combination with IMU and WO datasets, while optimizing the position, velocity and timing (PVT) computation in terms of integrity, accuracy, and convergence time.

The proposed method copes with highly varying LCNS visibility conditions and would significantly improve rover's navigation on the Moon's surface in regions where DTE is not achievable. Moreover, our results confirm that the LCNS would be a valuable source of information to be exploited in combination with onboard sensors to improve the accuracy of the reconstructed rover's traverse.

Keywords: Rover's navigation, Moon Exploration, Lunar Communication and Navigation Service, Extended Kalman Filter

1. Introduction

The lunar exploration represents a strategic priority to gain expertise and develop technical skills that will be the launching pad for future missions to Mars and to remote areas in the Solar System. The next generation exploration missions will be focused on developing and testing new technologies, completing science objectives, and exploiting *in situ* resources, paving the way for human exploration. Reliable navigation and communication capabilities are a fundamental requirement to succeed in these challenging goals. At the moment, lunar assets rely on Direct To Earth (DTE) links for communication and navigation [1,2]. This solution presents several drawbacks, *i.e.*, the user has to carry the necessary equipment to perform DTE communication, requiring increasing costs and large Size, Weight and Power (SWaP) demand. Moreover, the communication link can be established only when a ground station is in direct line of sight and available, limiting autonomous operations. An alternative technique for deep-space navigation is based on satellite-to-satellite tracking (SST). This method, which is well-suited for multispacecraft configurations, consists in combining SST observations and deep space tracking to provide spacecraft absolute orbit determination [3].

However, critical operations, *e.g.*, orbital maneuvers, final landing descent and rovers' traverses, require precise real-time navigation, which cannot be

accomplished through the processing of traditional Earth ground-based measurements. To make up for this lack, space agencies are making their very best effort to encourage the development of a centralized infrastructure that provides navigation and communication services in an efficient and cost-effective way [1].

In the next decades, the Lunar Communication and Navigation Service (LCNS), will serve a wide user ecosystem including platforms on and around the Moon, granting interoperability with other lunar infrastructures through a flexible and scalable architecture. Having a dedicated LCNS constellation would lead to unprecedented advantages to future missions enabling constant contact with Earth, even in case of DTE unavailability, *e.g.*, on the far side of the Moon.

The Moon's south polar region is one of the most interesting sites on the lunar surface due to the direct evidence of exposed water ice in permanently shadowed regions [4, 5, 6] (Fig. 1). The Nobile crater (sites 06 and DM2 in Fig. 1) and the Shackleton crater (site 04 in Fig. 1) are the selected landing sites of the next NASA lunar robotic missions, VIPER and PRIME 1 [7,8]. Therefore, we focused on the Shackleton crater, which is nearly coincident with the Moon's south pole and represents a promising candidate location to seek volatiles and ice [9].

To increase the rover's autonomy during science operations, path planning and traverse across harsh terrains, near real time positioning is a key requirement. We present here a method based on the Extended Kalman Filter (EKF) [10] that implements a multi model sensor fusion approach to estimate the surface user's position and velocity. The method has been validated in a realistic simulation scenario that includes an example of LCNS configuration and a robotic vehicle. The LCNS constellation has been optimized to offer a good coverage of the lunar south pole and provides one-way navigation signal. The rover is supposed to carry a user terminal that detects LCNS radio signals (*i.e.*, a functionality similar to GNSS receivers) and is able to process measurements collected by onboard sensors, which provide the distance travelled and the heading direction through Wheel Odometry (WO) and Inertial Measurement Unit (IMU), respectively.

The simulated rover's traverse was determined through an accurate dynamical modeling that accounts for both the deformability of the wheels and the terrain.

During LCNS visibility gaps, the rover's localization is accomplished through dead-reckoning methods. A kinematic model of the vehicle's motion is used to process IMU and WO data. Whenever pseudorange and pseudorange rates are available and at least three LCNS satellites are visible, these additional measurements are processed by the navigation filter in combination with IMU and WO datasets to guarantee acceptable positioning performances. Furthermore, to better constrain the rover's position, our method exploits the

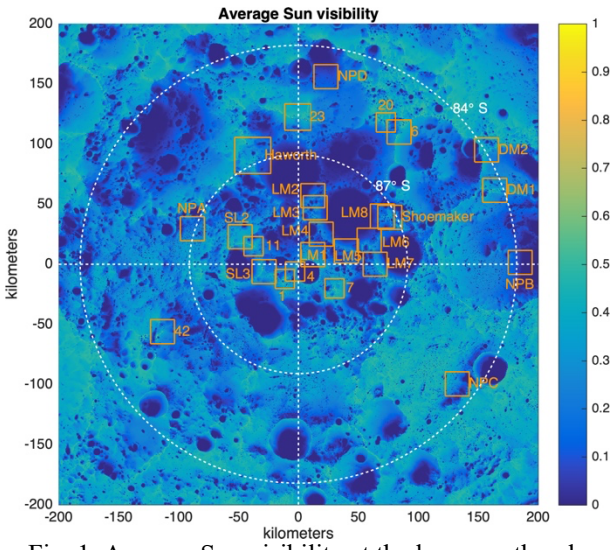

Fig. 1. Average Sun visibility at the lunar south pole (resolution: 240 m/pixel). The small squares mark the high-priority landing sites for which high-resolution 5 m/pixel DEMs have been derived. The projection is stereographic and centred at the south pole. Adapted from [6].

high-resolution Digital Elevation Models (DEMs) of the region of interest (ROI) derived using laser altimetry data acquired by LRO-LOLA [6].

The proposed method would significantly improve rover's navigation in regions where DTE is not achievable. Our results confirm that the combined processing of data coming from onboard sensors and LCNS user terminal would provide positioning accuracies $\lesssim$10 m on the horizontal plane.

In the next section we introduce the mission scenario; then we discuss the design of the localization filter. Finally, we show the results of our numerical simulations.

This publication does not cover the final Moonlight constellation, signals, and service, but rather presents what could be achieved with a lunar navigation satellite system. The actual Moonlight constellation, signal and related services will be defined as part of ESA programmes, and it is beyond the scope of this work.

2. Mission Scenario

The lunar surface user considered in our simulations is a rover located at coordinates $-89.703°$S, $130.429°$ E, and devoted to the exploration of the Shackleton crater (Fig. 2). The rover is moving along a planned traverse with constant steering angle and wheels speed $V \approx 0.403$ km/h, compatible with the expected VIPER's speed [11]. We considered an example of LCNS configuration that consists of four satellites in Elliptical Lunar Frozen Orbit (ELFO) [12].

This constellation offers a good coverage to the Moon's south pole (at latitudes ranging between 75°S–

90°S), maximizing the duration of visibility windows and optimizing the overall Geometric Dilution of Precision (GDOP) on the Moon's surface. The simulation covers six hours.

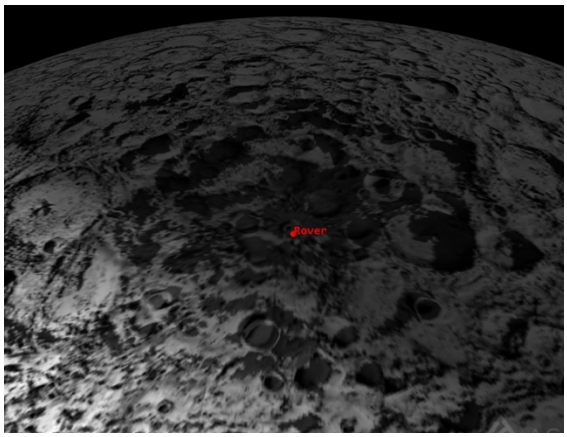

Fig. 2. Simulated mission scenario in STK, showing the rover in the Shackleton crater.

2.1 Navigation Payload and Measurement Modeling

The LCNS navigation payload is supposed to broadcast navigation messages to the lunar user assets. It was modelled as a nadir pointing antenna with isotropic gain pattern constrained within a 30° half cone from boresight. The carrier frequency is in the domain of the S-band [13], to avoid interference with GNSS L-band signals that might be exploited also by lunar assets [14]. The selected antenna parameters are reported in Table 1.

The user receiver pattern (Fig. 3) is assumed to be similar to GNSS receiving antennas. The user antenna is supposed to be zenith-pointed, by considering a Moon-Centred Moon-Fixed (MCMF) Frame.

Based on these settings, we performed visibility and link budget analysis and provided the C/N_0 estimate by using STK software.

LCNS one-way radio signals, pseudorange ρ and pseudorange rate $\dot{\rho}$, are modelled as follows:

$$\rho_r^S = \left|\left|r_r^S\right|\right| + \delta\tau_r - \delta\tau^S + \varepsilon_r^S \quad (1)$$

$$\dot{\rho}_r^S = \left|\left|\dot{r}_r^S\right|\right| + \dot{\delta}\tau_r - \dot{\delta}\tau^S + \dot{\varepsilon}_r^S \quad (2)$$

where the range r_r^S is the difference between the satellite and the receiver position vectors; the range rate $\dot{r}_r^S$ is the difference between the satellite and the receiver velocity vectors projected along the range direction; $\delta\tau_r$ and $\delta\tau^S$ are the receiver and the satellite clock errors in length unit $(c \cdot \delta t)$, respectively; and $\dot{\delta}\tau_r$ and $\dot{\delta}\tau^S$ are the receiver and the satellite clock error drifts, respectively. The pseudorange (ε_r^S) and pseudorange rate $(\dot{\varepsilon}_r^S)$ noises are modelled as zero mean white Gaussian noises considering that the pseudorange jitter assumes a Delay Lock Loop (DLL), while the Doppler measurements assume a Frequency Lock Loop (FLL). The associated standard deviations were computed by using the parameters reported in Table 2, as mentioned in [15],

$$\sigma_{DLL} = \lambda_c \sqrt{\frac{B_L d}{2C/N_0}\left(1 + \frac{1}{T_i C/N_0}\right)} \quad (3)$$

$$\sigma_{FLL} = \frac{\lambda_L}{2\pi T_i}\sqrt{\frac{4FB_L}{C/N_0}\left(1 + \frac{1}{T_i C/N_0}\right)}\,. \quad (4)$$

An additional error source depends on the Orbit Determination and Time Synchronization accuracy of the LCNS satellites. This quantity significantly affects the performances of the navigation filter, and its value is still uncertain. Therefore, we carried out a parametric study varying the contribution to the resulting Signal In Space Error (SISE).

Table 1. LCNS navigation payload characteristics

Parameter	Value
EIRP at boresight	11.5 dBW
Modulation	BPSK(10)
Carrier Frequency	2.491 GHz

Table 2. DLL and FLL parameters

Parameter	Value
Loop Bandwidth (B_L)	0.5 Hz
Coherent Integration (T_i)	20 ms
Early-late spacing (d)	1 chip
Wavelength (λ_L)	14.28 cm
Chip length (λ_c)	29.305 m
Factor (F) for high/low C/N0	1 or 2

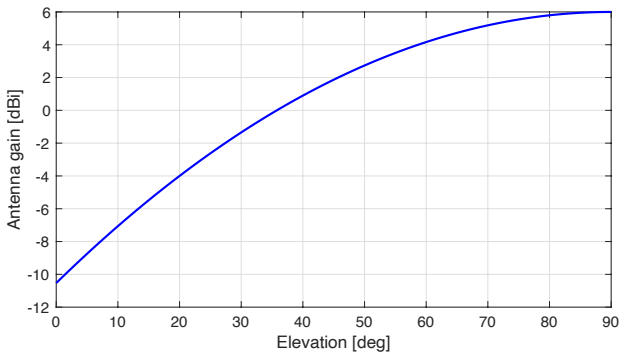

Fig. 3. User receiver antenna gain pattern

3. Simulated Rover's Traverse

The simulated rover's path was retrieved on the basis of an accurate dynamical modeling [16]. The characteristics of the ESA ExoMars rover's chassis and wheels were adapted to mimic the rover's locomotion on the low gravity Moon's surface. Soil properties, including cohesion, friction angle, exponent of terrain deformation, cohesive and frictional moduli, modulus of the shear deformation and density, are based on lunar regolith parameters [17].

The "Model for High-Speed Cornering" was assumed to describe the rover's motion. The integration of the full set of nonlinear equations describing the rover's dynamics allows to evaluate the rover's position, speed, yaw rate and heading direction by accounting for the contribution of the wheel-soil interaction forces [16].

However, this set of equations is only suitable to compute the rover's path on a fixed plane of motion. Therefore, we modified the approach presented in [16] and we included an accurate terrain modeling based on DEMs provided by Lunar Orbiter Laser Altimeter (LOLA) onboard the Lunar Reconnaissance Orbiter (Fig. 4) [6].

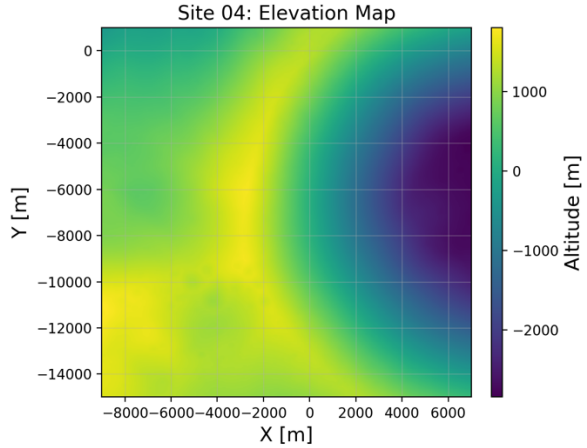

Fig. 4. Surface-interpolated elevation map of the Shackleton rim (Site 04). The heights of the surface points are referred to the International Astronomical Union (IAU) reference surface for the Moon (sphere of radius R = 1737.4 km). The projection is stereographic and centred at the south pole.

The steps of the method that we developed to compute the rover's traverse are described hereafter.

1. We define a reference frame, the Navigation Frame, centred at the initial rover's position with the X-axis pointing Eastwards, the Y-axis Northwards, and the Z-axis in the Up (*i.e.*, zenith) direction $(\hat{E}, \hat{N}, \hat{U})_{t_0}$ (Fig. 5) in the Moon's fixed frame MCMF.
2. At the beginning of each time step ($\Delta t_S = 30$ s), the rover's coordinates are computed in the MCMF frame $(\hat{X}_M, \hat{Y}_M, \hat{Z}_M)$ to evaluate the rover's longitude λ and latitude φ.
3. The values (λ, φ) are converted into stereographic coordinates (X_s, Y_s) and the corresponding cell on the DEM is identified.
4. The 8 DEM cells surrounding the rover's position are identified. By using the information on the terrain altitude, the slope β and the aspect α (*i.e.*, the downslope direction, measured clockwise from the North), are computed with a 24 m baseline.
5. The surface normal vector in ($\hat{E}, \hat{N}, \hat{U}$) components [18] is evaluated as:

$$\hat{n} = \begin{bmatrix} \sin(\alpha)\sin(\beta) \\ \cos(\alpha)\sin(\beta) \\ \cos(\beta) \end{bmatrix} \quad (5)$$

6. The Rover's Body Frame is defined as $(\hat{x}_B, \hat{y}_B, \hat{z}_B)$ (Fig. 6). At time t_i the normal vector $\hat{n}_{t_i}$ is aligned with the rover's body axis $\hat{z}_{B_{t_i}}$ .The rover's body axis $\hat{x}_{B_{t_i}}$ identifies the rover's heading direction.
   $\hat{x}_{B_{t_i}}$ is computed as the projection of $\hat{x}_{B_{t_{i-1}}}$, (*i.e.*, the rover's longitudinal axis at the end of the previous step), on the new plane of motion characterized by the normal vector $\hat{n}_{t_i}$. $\hat{y}_{B_{t_i}}$ completes the right-handed orthonormal basis.
7. The rover's state is integrated in the frame that coincides with the Rover's Body Frame at the beginning of each time interval Δt_s with an integration time interval $\Delta t = 1$ s.

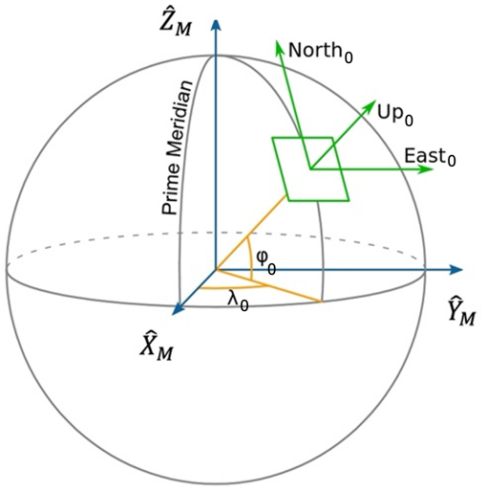

Fig. 5. Reference frames: definition of the Navigation Frame with respect to the Moon-Centred Moon-Fixed Frame

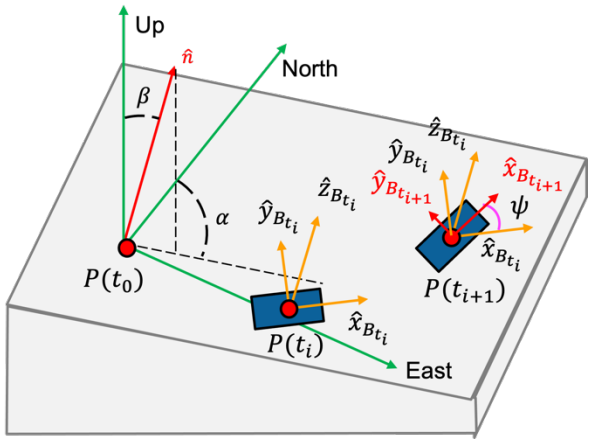

Fig. 6. Representation of the Rover's Body frame with respect to the Navigation Frame

At the end of each step Δt_s, the rover's coordinates and the speed are re-projected in the Navigation Frame. The rover's longitudinal axis at the end of the motion step is computed by rotating the $\hat{x}_{B_{t_i}}$ axis about the $\hat{z}_{B_{t_i}}$ axis by an angle equal to the change in heading direction.

The simulated traverse is shown in Fig. 7.

4. Navigation Filter

The proposed navigation algorithm adopts a multi-modal sensor fusion approach. The rover's state is updated through a joint processing of dead-reckoning and LCNS data, accounting for satellites' visibility from the surface. The state vector $\hat{x} = [X, Y, Z, \dot{X}, \dot{Y}, \dot{Z}, \delta\tau, \dot{\delta\tau}]^T$ includes the rover's position and velocity in the Navigation Frame and the receiver's clock bias and drift. WO and IMU provide the wheels' commanded speed $\bar{V}$ and the heading direction $\bar{x}_B$. These measurements are processed with a time step $\Delta t = 1$ s. The measurement noise is modelled as zero-mean white Gaussian with standard deviations $\sigma_{WO} = 1$ cm/s (*i.e.*, ~10% of the rover's commanded sped) and $\sigma_{IMU} = 0.05°$, respectively. The values that we used in our simulation represent a conservative assumption since space qualified IMUs present better attitude and velocity accuracies ($< 0.01°$ and 5 mm/s [19]). However, under normal conditions wheel odometry accuracy is not better than 10% of the distance travelled, leading to worse performances in higher slip environments [20].

The state update is performed at each step through dead reckoning, *i.e.*, by adopting a kinematic modeling:

$$x_{K+1} = f(\hat{x}_K, \bar{V}, \bar{x}_B) = \begin{cases} X_{K+1} = \hat{X}_K + \hat{\dot{X}}_K \Delta t \\ Y_{K+1} = \hat{Y}_K + \hat{\dot{Y}}_K \Delta t \\ Z_{K+1} = \hat{Z}_K + \hat{\dot{Z}}_K \Delta t \\ \dot{X}_{K+1} = \bar{V}_{K+1}\, \bar{x}_{B1_{K+1}} \\ \dot{Y}_{K+1} = \bar{V}_{K+1}\, \bar{x}_{B2_{K+1}} \\ \dot{Z}_{K+1} = \bar{V}_{K+1}\, \bar{x}_{B3_{K+1}} \\ \delta\tau_{K+1} = \widehat{\delta\tau}_K + \widehat{\dot{\delta\tau}}_K \Delta t \\ \dot{\delta\tau}_{K+1} = \widehat{\dot{\delta\tau}}_K \end{cases} \quad (6)$$

The covariance matrix is updated according to:

$$P_{K+1} = F_x\, \hat{P}_K F_x^T + Q \quad (7)$$

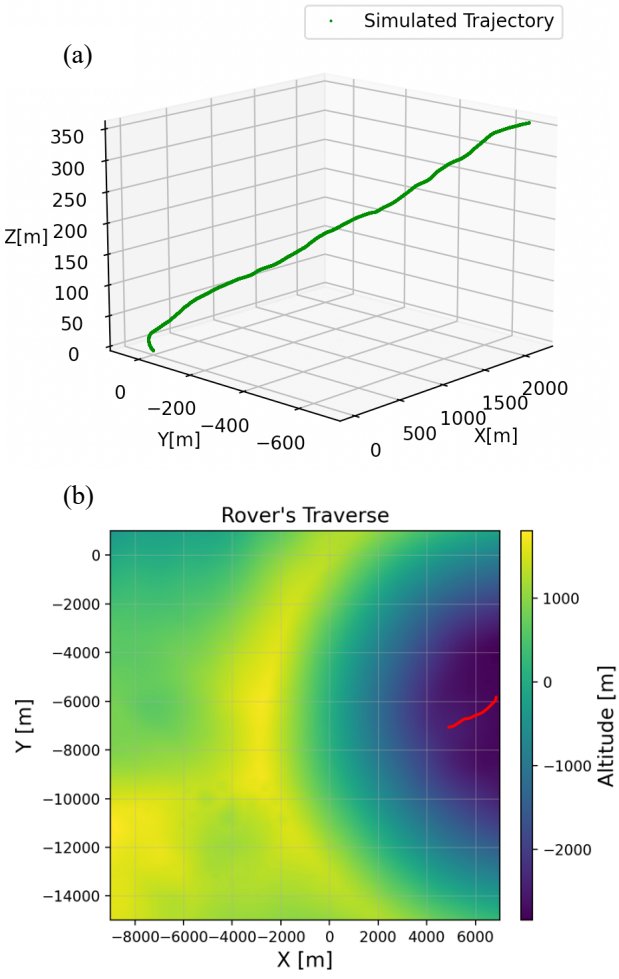

Fig. 7. Simulated rover's traverse. (a) Rover's path in the Navigation Frame $(\hat{E}, \hat{N}, \hat{U})|_{t_0}$. (b) Elevation map and simulated traverse (red) projected in the stereographic frame.

Table 3. Navigation Filter setup: uncertainties.

Parameter	State Vector Element	Value
Process Noise Q (1σ)	Position (σ_p)	0.10 m
	Velocity (σ_v)	0.01 m/s
	Clock Bias (σ_τ)	10 m
	Clock Drift $(\sigma_{\dot{\tau}})$	0.1 m/s
Initial Covariance P_0 (1σ)	Position	50 m
	Velocity	0.01 m/s
	Clock Bias	100 m
	Clock Drift	1 m/s

where F_x is the state transition matrix,

$$F_x = \begin{bmatrix} I_{3\times3} & I_{3\times3} & 0_{3\times1} & 0_{3\times1} \\ 0_{3\times3} & 0_{3\times3} & 0_{3\times1} & 0_{3\times1} \\ 0_{1\times3} & 0_{1\times3} & 1 & \Delta t \\ 0_{1\times3} & 0_{1\times3} & 0 & 1 \end{bmatrix}, \quad (8)$$

and Q is the process noise matrix, assumed to be diagonal:

$$Q = \begin{bmatrix} \sigma_p^2 & 0 & 0 & 0 & 0 & 0 & 0 & 0 \\ 0 & \sigma_p^2 & 0 & 0 & 0 & 0 & 0 & 0 \\ 0 & 0 & \sigma_p^2 & 0 & 0 & 0 & 0 & 0 \\ 0 & 0 & 0 & \sigma_v^2 & 0 & 0 & 0 & 0 \\ 0 & 0 & 0 & 0 & \sigma_v^2 & 0 & 0 & 0 \\ 0 & 0 & 0 & 0 & 0 & \sigma_v^2 & 0 & 0 \\ 0 & 0 & 0 & 0 & 0 & 0 & \sigma_\tau^2 & 0 \\ 0 & 0 & 0 & 0 & 0 & 0 & 0 & \sigma_{\dot{\tau}}^2 \end{bmatrix} \quad (9)$$

The values adopted in the process noise matrix and in the initial covariance matrix P_0 are reported in Table 3.

By using the kinematic model of the vehicle motion in the path reconstruction, the rover's speed is assumed to be aligned with the rover's heading direction, and the wheels' slippage is not considered. On the contrary, the simulated trajectory of the rover was computed adopting the dynamical modeling that includes the wheels' slippage in the generation of the rover's motion. Therefore, the assumptions of dead-reckoning lead to a poor reconstruction of the rover's traverse and the error on the position estimate increases continuously.

During the visibility intervals, *i.e.*, when at least three LCNS satellites are visible and the link budget constraint of a C/N_0 greater than 30 dB/Hz threshold is satisfied, the 1-way radio signals are processed through the EKF. To compensate inversion stability due to the limit of the satellites that are visible from the rover, the vertical position of the asset is provided by the DEM, which is treated as an additional observable.

The vector of the computed observables h is defined as follows:

$$h = [\rho_r^{S1}, \dots, \rho_r^{SN}, \dot{\rho}_r^{S1}, \dots, \dot{\rho}_r^{SN}, Z - h_{DEM}]^T \quad (10)$$

where h_{DEM} is the DEM topographic relief reprojected along the radial direction of the Navigation Frame $\widehat{U}$, and N is the number of available satellites that varies between 3 and 4.

The estimated range $||r_r^S||$ and range rate $\left|\left|\dot{r}_r^S\right|\right|$ are computed at each step:

$$\left|\left|r_r^S\right|\right| = \sqrt{(X_S - X)^2 + (Y_S - Y)^2 + (Z_S - Z)^2} \quad (11)$$

$$\left|\left|\dot{r}_r^S\right|\right| = \frac{X_S - X}{||r_r^S||}\left(\dot{X}_S - \dot{X}\right) + \frac{Y_S - Y}{||r_r^S||}\left(\dot{Y}_S - \dot{Y}\right) + \frac{Z_S - Z}{||r_r^S||}\left(\dot{Z}_S - \dot{Z}\right) \quad (12)$$

The vector of the observed observables, z, is defined as:

$$z = [\bar{\rho}_r^{S1}, \dots, \bar{\rho}_r^{SN}, \bar{\dot{\rho}}_r^{S1}, \dots, \bar{\dot{\rho}}_r^{SN}, -h_0]^T \quad (13)$$

where h_0 is the DEM topographic height evaluated in the initial rover's coordinates.

Therefore, the matrix H, which contains the partial derivatives of the computed observables with respect to the state vector, is defined as follows:

$$H = \begin{bmatrix} \frac{\partial \rho_r^{S1}}{\partial r_r} & \frac{\partial \rho_r^{S1}}{\partial \dot{r}_r} & \frac{\partial \rho_r^{S1}}{\partial \tau_r} & \frac{\partial \rho_r^{S1}}{\partial \dot{\tau}_r} \\ \vdots & \vdots & \vdots & \vdots \\ \frac{\partial \rho_r^{SN}}{\partial r_r} & \frac{\partial \rho_r^{SN}}{\partial \dot{r}_r} & \frac{\partial \rho_r^{SN}}{\partial \tau_r} & \frac{\partial \rho_r^{SN}}{\partial \dot{\tau}_r} \\ \frac{\partial \dot{\rho}_r^{S1}}{\partial r_r} & \frac{\partial \dot{\rho}_r^{S1}}{\partial \dot{r}_r} & \frac{\partial \dot{\rho}_r^{S1}}{\partial \tau_r} & \frac{\partial \dot{\rho}_r^{S1}}{\partial \dot{\tau}_r} \\ \vdots & \vdots & \vdots & \vdots \\ \frac{\partial \dot{\rho}_r^{SN}}{\partial r_r} & \frac{\partial \dot{\rho}_r^{SN}}{\partial \dot{r}_r} & \frac{\partial \dot{\rho}_r^{SN}}{\partial \tau_r} & \frac{\partial \dot{\rho}_r^{SN}}{\partial \dot{\tau}_r} \\ 0 & 0 & 1 & 0 \end{bmatrix} \quad (14)$$

The Kalman gain can be computed accordingly to:

$$K_{K+1} = P_{K+1} H_{K+1}^T \left(H_{K+1} P_{K+1} H_{K+1}^T + R_{yy_{K+1}} \right)^{-1} \quad (15)$$

where R_{yy} represents the measurement covariance matrix and includes the contribution of the LCNS ephemeris error, the thermal noise associated with the pseudo-range and pseudo-range rate measurements and the vertical position uncertainty related to the DEM:

$$R_{yy} = diag\left[\sigma_{\rho 1}^2, \dots, \sigma_{\rho N}^2, \sigma_{\dot{\rho} 1}^2, \dots, \sigma_{\dot{\rho} N}^2, \sigma_{DEM}^2\right] \quad (16)$$

where,

$$\sigma_{\rho_i}^2 = \sigma_{DLL_i}^2 + \sigma_p^{Si\,2} + \sigma_\tau^{Si\,2} \quad (17)$$

$$\sigma_{\dot{\rho}_i}^2 = \sigma_{FLL_i}^{\;2} + \sigma_v^{Si\,2} + \sigma_{\dot{\tau}}^{Si\,2} \quad (18)$$

The selected values of uncertainties on the LCNS satellites position σ_p^{Si} and velocity σ_v^{Si} range from 5 m to 50 m, and from 0.05 m/s to 0.5 m/s, while the uncertainty on the transmitter clock bias and drift have been set equal to $\sigma_\tau^{Si} = 10$ m and $\sigma_{\dot{\tau}}^{Si} = 0.1$ m/s.

The uncertainty on the local DEM can be evaluated as the sum of two components; the first one is $\sigma_{DEM,1}$ and it is related to the DEM generation process. The second term $\sigma_{DEM,2}$ accounts for the uncertainty on the rover's position and its impact on the selection of the corresponding cell in the DEM.

$$\sigma_{DEM}^2 = \sigma_{DEM,1}^2 + \sigma_{DEM,2}^2 \quad (19)$$

The first term can be directly extracted from the uncertainty matrix available at [6]. As shown in Fig. 8, $\sigma_{DEM,1}$ is below 1 m in almost the whole Site 04 area.

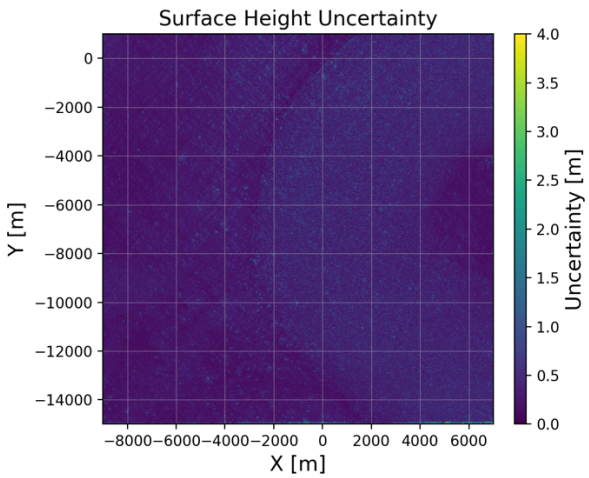

Fig. 8. Local DEM uncertainty projected in the stereographic frame across the Site 04.

(a) $(\lambda - d\lambda, \phi + d\phi)$	(b) $(\lambda, \phi + d\phi)$	(c) $(\lambda + d\lambda, \phi + d\phi)$
(d) $(\lambda - d\lambda, \phi)$	(e) (λ, ϕ)	(f) $(\lambda + d\lambda, \phi)$
(g) $(\lambda - d\lambda, \phi - d\phi)$	(h) $(\lambda, \phi - d\phi)$	(i) $(\lambda + d\lambda, \phi - d\phi)$

Fig. 9. 3×3 matrix that identifies the cells of the DEM representing the region used to compute the $\sigma_{DEM,2}$. uncertainty.

The rover's traverse is projected in the Navigation Frame, while the DEM of the ROI is projected in the stereographic frame centred in the Moon's south pole. Therefore, to evaluate the contribution of $\sigma_{DEM,2}$ several steps are required. The proposed procedure represents a conservative approach. First, the latitude ϕ and longitude λ of the estimated rover's position are computed (point e in the matrix in Fig. 9). Then, the radius of the uncertainty circle d on the horizontal plane is computed as the maximum between the uncertainties along the $\hat{E}$ and $\hat{N}$ axes:

$$d = \max\left(\sqrt{P_{11}}, \sqrt{P_{22}}\right) \quad (20)$$

The distance d is converted into a displacement in terms of longitude $\delta\lambda$ and latitude $\delta\phi$ and the 8 points surrounding the estimated rover's coordinates are identified (Fig. 9). For each point of the 3×3 matrix

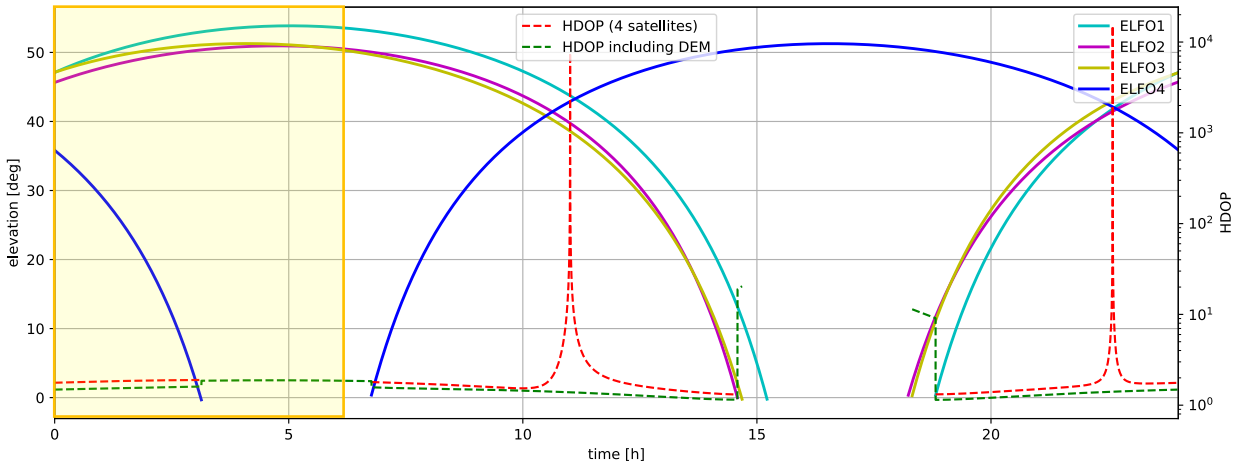

Fig. 10. Evolution of the elevation angles of the four LCNS ELFO satellites during a 24 h time window with respect to an observer located in the Moon's south pole at latitude $\lambda = -89.703°$S and longitude $\phi = 130.429°$ E. The dashed lines represent the *HDOP* computed by using the standard formulation [15] which only applies when four LCNS satellites are visible (red) and by including the DEM altitude information when also only three satellites are available (green).

the stereographic coordinates are computed and the maximum distance d_{max} from central point is evaluated.

The cells that are included in the squared region having side equal to d_{max} and centred at the estimated rover's position are considered to compute the standard deviation of the DEM, which represents the value $\sigma_{DEM,2}$.

Finally, the state and the covariance matrix are updated accordingly to:

$$\hat{x}_{K+1} = x_{K+1} + K_{K+1}(z_{K+1} - h_{K+1}) \quad (21)$$

$$\hat{P}_{K+1} = (I - K_{K+1}H_{K+1})P_{K+1}(I - K_{K+1}H_{K+1})^T + \\ + K_{K+1}R_{yy_{K+1}}K_{K+1}^T \quad (22)$$

The Horizontal Dilution of Precision (HDOP), which measures the informative contribution of the range observables on the horizontal plane, is computed as follows:

$$A = \begin{bmatrix} \frac{\partial \rho_r^{S1}}{\partial r_r} & \frac{\partial \rho_r^{S1}}{\partial \tau_r} \\ \vdots & \vdots \\ \frac{\partial \rho_r^{SN}}{\partial r_r} & \frac{\partial \rho_r^{SN}}{\partial \tau_r} \\ [0,0,1] & 0 \end{bmatrix} \quad (23)$$

$$\bar{A} = (A^T A)^{-1} \quad (24)$$

$$HDOP = \sqrt{\bar{A}_{11} + \bar{A}_{22}} \quad (25)$$

When the number of available LCNS satellites is $N = 3$, only three pseudo-ranges ρ and pseudo-range rates $\dot{\rho}$ are available. By using the constraint on the rover's vertical position, a maximum set of 7 components of the rover's state can be evaluated. Therefore, the smaller component of the rover's speed, *i.e.*, the radial one, $\dot{Z}$ is not updated through the EKF, and it is evaluated only through the kinematic modeling. The column of the H matrix corresponding to the derivative of the computed observables with respect to the state vector component $\dot{Z}$ is eliminated. Furthermore, the adopted formulation allows computing the $HDOP$ value also when only 3 satellites are visible.

Any time the number of available satellites changes from three to four or viceversa, the covariance matrix is re-initialized and set equal to P_0.

5. Results

In Fig. 10 we show the estimated $HDOP$ provided by the LCNS configuration for a rover in the Shackleton crater ($\lambda = -89.703°$S, $\phi = 130.429°$ E) during a 24 h time window, when at least 3 satellites are available and the constraint on the minimum C/N_0 is satisfied. In this picture we superimpose the $HDOP$ evolution on the pattern of the LCNS satellites elevation angles.

The red line represents the $HDOP$ that can be evaluated only in the case of four available LCNS satellites without including DEM measurements. As soon as the elevation angles of the available satellites is simultaneously above 45° there is a degradation of the information that the observables can provide on the rover's position on the horizontal plane. This process can also be observed in the value of $HDOP$, that suddenly increases up to 10^4. However, most of the time the $HDOP$ reaches values below 2, suggesting a good characterization of the accuracy of the position/time solution. The adoption of

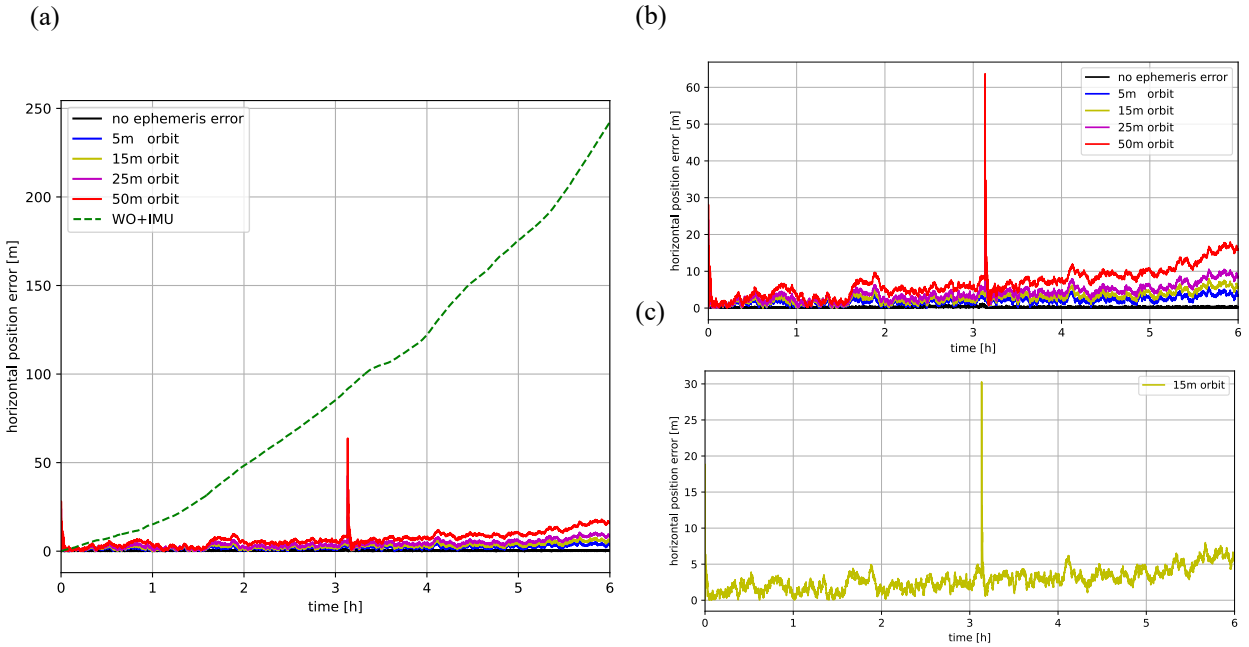

Fig. 11. Horizontal position error in meters. (a) Results obtained during the 6-h traverse with dead-reckoning (green line) and with the EKF including different levels of ODTS uncertainties are compared. (b) Zoom-in of the EKF solutions, (c) and of the most realistic case, *i.e.*, LCNS position uncertainty $\sigma_p^{Si} = 15$ m, velocity uncertainty $\sigma_v^{Si} = 0.15$ m/s and clock bias and drift uncertainties $\sigma_\tau^{Si} = 10$ m and $\sigma_{\dot{\tau}}^{Si} = 0.1$ m/s. In this case the error is always $\leq$ 5m when 4 LCNS satellites are available, and $\leq$ 10 m with only 3 visible LCNS satellites.

the $HDOP$ definition that includes the DEM contribution (eq. 23-25) leads to a significant improvement that can be observed in the green line in Fig. 10; the peaks that characterize the red line completely disappear, and the solution can be computed also in case of only three LCNS visible satellites. The $HDOP$ computed with only 3 LCNS satellites is slightly worse than the one obtained during visibility intervals that include 4 LCNS satellites.

The simulated rover's traverse covers six hours and corresponds to the time window highlighted in Fig. 10. The resulting positioning errors computed on the horizontal plane by using IMU and WO dataset only, and by using the EKF with different levels of LCNS ODTS uncertainties are compared in Fig. 11-a. As expected, the kinematic assumption and the noisy IMU and WO measurements cause a strong mismodeling, and the horizontal position error (green dashed line) continuously accumulates over time.

Looking at the curves obtained processing the additional observables, *i.e.*, ranges, range rates and DEM measurements, the error on the horizontal plane significantly decreases. Fig. 11-b shows that with increasing uncertainty on the LCNS position, velocity and timing solution, the estimate of the rover's position considerably worsens. In Fig. 11-c, we focus on the solution that includes 15 m and 0.15 m/s uncertainties on the LCNS position and velocity vectors, respectively. These values are the same adopted in other works [2, 21, 22] and represent the achievable accuracies at maximum age-of-data (AOD) [23]. With this assumption, we obtain a horizontal position error that never exceeds 7 m, except for the two peaks that coincide with the filter initializations. In the first part of the simulation (from 0 to ~3 hours), the solution is computed using observables collected from four LCNS satellites, and during this phase the rover's position error is always $\leq$ 5 m. Then, when the ELFO 4 satellite sets below the horizon, the filter is re-initialized, and the solution is evaluated with the three satellites left, leading to a slightly higher value of the horizontal error.

The 3σ formal uncertainties on the horizontal position are reported in Fig. 12. The IMU+WO solution (green dashed) confirms a poor estimate of the rover's position with an uncertainty that increases leading to a standard deviation >200 m at the end of the traverse. The EKF used in the other cases yields lower uncertainties that increase with the increased values of LCNS ODTS uncertainties. The peaks at $t = 0$ h and at $t \simeq 3.2$ h result from the filter re-initialization. The uncertainty, which is below 8 m in the more realistic case (yellow), is compatible with the estimated position error.

The $3-\sigma$ formal uncertainties on the horizontal velocity shown in Fig. 13 suggest that the LCNS radio signals do not significantly improve the rover's velocity estimate. Indeed, the uncertainty on the horizontal

velocity is driven by the WO expected accuracy and it is strongly affected by the σ_{FLL} value, which is ~4.5 cm/s.

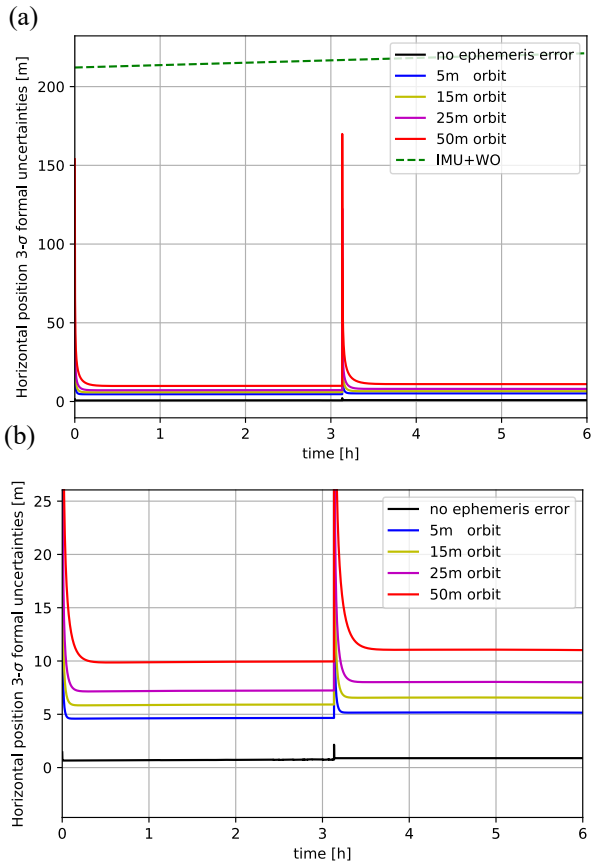

Fig. 12. (a) $3-\sigma$ formal uncertainties associated with the rover's horizontal position estimate, (b) zoom-in of the EKF solutions.

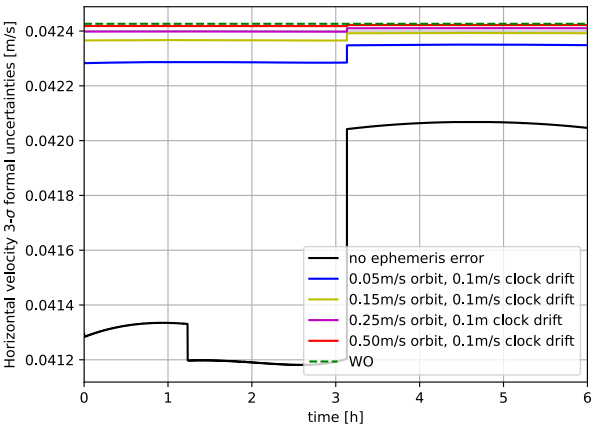

Fig. 13. $3-\sigma$ formal uncertainties associated with the rover's horizontal velocity estimate.

Finally, in Fig. 14 we show a close-up of the computed $HDOP$ during the 6-hours rover's traverse. The $HDOP$ value increases reaching 1.6 during the time interval in which four ELFO satellites are visible, and then suddenly increases up to 1.87 when only 3 satellites are available.

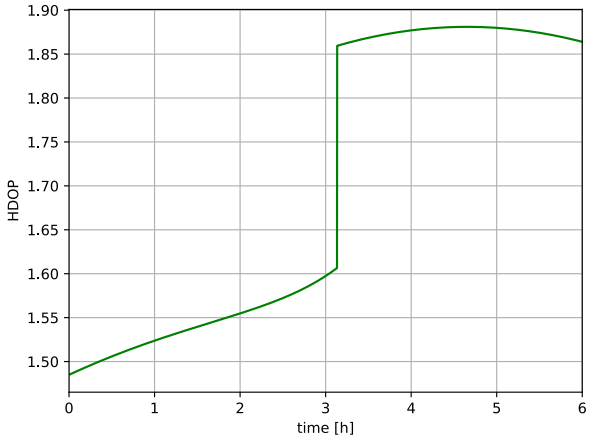

Fig. 14. Estimated $HDOP$ during the 6-h rover's traverse

6. Conclusions and Future Works

The main goal of this work was the development of a method to evaluate the achievable position and velocity accuracies for a lunar surface user located in the Moon's south polar region by jointly using a dedicated Lunar Communication and Navigation Service and data collected by the onboard sensors.

The design and development of the LCNS is included in the Moonlight initiative and space agencies are working along with industrial partners to provide efficient navigation and telecommunication services to lunar assets. The LCNS is expected to broadcast one-way radio signals similarly to Earth GNSS systems, involving a high degree of technology reuse and reduced time to market. This dedicated constellation would guarantee service availability in all illumination conditions and even in case of Direct To Earth link unavailability, *i.e.*, on the far side of the Moon or in the south polar region.

In this work, we considered an orbital configuration that includes four ELFO satellites and represents an example of LCNS constellation. The rover, which hosts onboard the user terminal, is supposed to explore the rim of the Shackleton crater, one of the most interesting sites of the Moon's south polar region from the geological point of view [24]. The rover is also equipped with fundamental instruments that provide the rover's speed and the heading direction, *i.e.*, wheel encoders and IMU, respectively. The assumptions made in our simulations to model the accuracies of WO and IMU measurements and the LCNS ODTS performances represent a conservative approach. Indeed, the uncertainties associated with IMU and WO are in line with the expected wheel odometry performances; the ODTS accuracy of the LCNS satellites considered in this work ranges from 5 m and 0.05 m/s to 50 m and 0.5 m/s for position and velocity and assumes

10 m and 0.1 m/s uncertainties on clock bias and drift. Therefore, in our simulations we are also taking into account the worst-case scenario with a poor LCNS orbit prediction. Furthermore, we are including a minimum set of instruments that are commonly onboard space exploration rovers (IMU+WO). The scenario that we analysed represents a baseline that might be further investigated by exploiting observables from other sensors, *i.e.*, stereo cameras (Visual Odometry (VO)) [25, 26] and LiDAR [27].

The navigation filter that we developed adopts a multi modal/cooperative sensor fusion approach to process IMU and WO datasets collected onboard and LCNS radio signals when more than two satellites are available. These measurements were simulated by accounting for an accurate dynamical model of the rover that includes the deformability of both the wheels and the terrain [16], and a precise reconstruction of the lunar terrain by using the available high resolution Digital Elevation Models [6]. By introducing the knowledge of the topographic relief where the rover is initially located and the DEM measurements as additional observables in the Extended Kalman Filter, the estimation of the rover's state is better constrained, and the filter performances are enhanced.

The results show that in the most realistic case, *i.e.*, assuming $1-\sigma$ uncertainties on the LCNS satellites position, velocity and clock bias and drift equal to 15 m, 0.15 m/s, 10 m and 0.1 m/s respectively, the 3-σ formal uncertainties on the rover's horizontal position and velocity reach values that are below 8 m and 0.043 m/s, respectively. These results suggest that the LCNS would be a valuable source of information to be exploited in combination with onboard sensors to significantly improve the reliability of the reconstructed rover's path. Our navigation algorithm fully supports rover's autonomous navigation on the lunar surface and the increasingly challenging objectives of the next exploration missions.

Future works will be focused on the integration of additional sensors datasets to improve the accuracy of the navigation filter's solution and the development of autonomous path planning and obstacle avoidance strategies.

References

[1] ESA. Lunar Satellites. 2020, https://www.esa.int/Applications/Telecommunications_Integrated_Applications/Lunar_Satellites, (accessed 01.02.2022).

[2] P. Giordano et al., Moonlight navigation service-how to land on peaks of eternal light, IAC-21-B2.6.5, 72nd International Astronautical Congress Dubai, United Arab Emirates, 2021.

[3] A. Genova and F. Petricca, Deep-space navigation with intersatellite radio tracking. J. Guid. Control Dyn. 44 (2021) 1068-1079.

[4] P. D. Spudis et al., Evidence for water ice on the Moon: Results for anomalous polar craters from the LRO Mini- RF imaging radar. JGR Planets, 118, (2013) 2016-2029.

[5] S. Li et al., Direct evidence of surface exposed water ice in the lunar polar regions. PNAS, 115 (2018) 8907-8912.

[6] M.K. Barker et al., Improved LOLA Elevation Maps for South Pole Landing sites: Error Estimates and their impact on Illumination Conditions, Planet. Space Sci. 203 (2021) 105119.

[7] J. Handal, K. Fox, K. Cousins, NASA's Artemis Rover to Land Near Nobile Region of Moon's South Pole. 20 September 2021, https://www.nasa.gov/press-release/nasa-s-artemis-rover-to-land-near-nobile-region-of-moon-s-south-pole, (accessed 13.07.22).

[8] H. Smith, NASA, Intuitive Machines Announce Landing Site Location for Lunar Drill. 3 November 2021, https://www.nasa.gov/feature/nasa-intuitive-machines-announce-landing-site-location-for-lunar-drill, (accessed 13.07.22).

[9] M.T. Zuber, J.W. Head, D.E. Smith, G.A. Neumann, E. Mazarico, M.H. Torrence, O. Aharonson, A.R. Tye, C.I. Fasset, M.A. Rosenburg, H.J. Melosh, Constraints on the volatile distribution within Shackleton crater at the lunar south pole, Nature 486 (2012) 378–381.

[10] B. D. Tapley, B. E. Schutz and G. H. Born, Statistical Orbit Determination, Elsevier Academic Press, London, 2004.

[11] R. Chen, NASA, VIPER: The Rover and Its Onboard Toolkit. 17 February 2022, https://www.nasa.gov/viper/rover, (accessed 13.07.22).

[12] D. Folta and D. Quinn, Lunar Frozen Orbits. AIAA 2006-6749. AIAA/AAS Astrodynamics Specialist Conference and Exhibit. August 2006.

[13] Space Frequency Coordination Group. Communication AND Positioning, Navigation, and Timing Frequency Allocations and Sharing in the Lunar Region, 2021. Available online: https://www.sfcgonline.org/Recommendations/REC%20SFCG%2032-2R3%20(Freqs%20for%20Lunar%20region).pdf (accessed on 22 July 2022).

[14] A. Delépaut, A. Minetto, F. Dovis, F. Melman, P. Giordano, J. Ventura-Travaset, Enhanced GNSS-based Positioning in space exploiting Inter-Spacecraft Cooperation. Proceedings of the 2022 International Technical Meeting of the Institute of Navigation, Long Beach, California, 2022, January 25-27.

[15] E. D. Kaplan and C. J. Hegarty. Understanding GPS, Principles and Applications, Artech House, 2006.

[16] A.M. Gargiulo, I. di Stefano and A. Genova, A model based slippage estimation to enhance planetary rover localization with wheel odometry. Appl. Sci. 11 (2021) 5490.

[17] G. Genta. Introduction to the Mechanics of Space Robots, 1st ed., Springer, Dordrecht, The Netherlands, 2012.

[18] M. E. Hodgson, L. Gaile, A cartographic modeling approach for surface orientation-related applications. Photogramm. Eng. Rem. S. , 65 (1999) 85-95.

[19] iMAR. iNAV-RQH-1001, 2014. Available online: https://www.imar-navigation.de/downloads/NAV_RQH_1001_en.pdf 742 (accessed 11.07.2022).

[20] D. M. Helmick, Y. Cheng, D. S. Clouse, L. H. Matthies and S. I. Roumeliotis, Path following using visual odometry for a Mars rover in high-slip environments. 2004 IEEE Aerospace Conference Proceedings, 2004, pp. 772-789 Vol.2.

[21] Grenier, A.; Giordano, P.; Bucci, L.; Cropp, A.; Zoccarato, P.; Swinden, R.; Ventura-Traveset, J. Positioning and Velocity Performance Levels for a Lunar Lander using a Dedicated Lunar Communication and Navigation System. NAVIGATION: Journal of the Institute of Navigation 2022, 69.

[22] F.T. Melman, P. Zoccarato, C. Orgel, R.D. Swinden, P. Giordano, J. Ventura-Traveset, LCNS Positioning of a Lunar Surface Rover Using a DEM Based Altitude Constraint. Preprints 2022, 2022070236, (doi: 10.20944/preprints202207.0236.v1).

[23] European Commission. European GNSS (Galileo) Open Service Definition Document, 2021. Available online: https://www.gsc- 753 europa.eu/sites/default/files/sites/all/files/Galileo-OS-SDD_v1.2.pdf (accessed 14.07.2022).

[24] P. D. Spudis, B. Bussey, J. Plescia, J.-L. Josset, and S. Beauvivre, Geology of Shackleton Crater and the south pole of the Moon, Geophys. Res. Lett., 35 (2008).

[25] S. Andolfo, F. Petricca, A. Genova, Rovers Localization by using 3D-to-3D and 3D-to-2D Visual Odometry. In Proceedings of the IEEE 8th International Workshop on Metrology for AeroSpace, Naples, Italy, 23–25 June 2021

[26] S. Andolfo, F. Petricca, A. Genova, Visual Odometry analysis of the NASA Mars 2020 Perseverance rover's images. In Proceedings of the IEEE 9th International Workshop on Metrology for AeroSpace, Pisa, Italy, 27–29 June 2022.

[27] A.M. Gargiulo, I. di Stefano, A. Genova, Numerical Simulations for Planetary Rovers Safe Navigation and LIDAR Based Localization. In Proceedings of the IEEE 8th International Workshop on Metrology for AeroSpace, Naples, Italy, 23–25 June 2021.